Supporting information

Trehalose-enhanced Anti-Freezing Conductive Hydrogels with High Stretchability and Low Hysteresis for Flexible Human-Machine Interaction

Fangying Lu [a,b], *Jingye Liang* [a,b], *Xiya Shan* [a,b], *Hanbing Yu* [a,b], *Yiqiong Zhang* [a,b], *Qian Ji* [a,b], *Aoyun Ren* [a,b], *Run Wang* [a,b]*

[a]Ministry of Education Key Laboratory of Advanced Textile Composite Materials, Institute of Composite Materials, Tiangong University, 399 West Binshui Road, Tianjin 300387, China.

[b]School of Textile Science and Engineering, Tiangong University, 399 West Binshui Road, Tianjin 300387, China.

Corresponding author E-mail: wangrun@tiangong.edu.cn

Experimental Section

Materials

Acrylamide (AM), polyvinyl alcohol (PVA) and trehalose were from Aladdin (Shanghai, China). N, N′-methylene-bis-acrylamide (MBAA), and ammonium persulfate (APS) were from Shanghai Yi'en Chemical Technology Co., Ltd (Shanghai, China). Lithium chloride (LiCl) was from Bide Pharmatech Co., Ltd (Shanghai, China). All chemicals were used without further purification.

Preparation of PAM/PVA/Tre/Li^+ hydrogels

PAM/PVA/Tre/Li^+ hydrogel was prepared by the one-pot free radical polymerization method. First, AM (3.00 g), PVA (0.15 g), trehalose (0.60 g), and LiCl (0.30 g), were added into deionized water (total mass of 11.05 g). The mixture was magnetically stirred in a 90.0°C water bath for 1 h to ensure uniformity, and then the solution was cooled to room temperature. Then APS (0.06 g) and MBAA (0.03 g) were added to the above solution, and the solution was stirred at room temperature until dissolved. The solution was poured into the mold and placed in the oven at 60.0°C for 2 h to induce free radical polymerization to prepare PAM/PVA/Tre/Li^+ hydrogel. Other hydrogels were prepared by the same method, different mass fractions of trehalose and LiCl added relative to the acrylamide monomer.

Preparation of strain sensors and smart glove

The hydrogel strain sensor was rectangular with a length of 20 mm, a width of 5 mm and a thickness of 1 mm. Subsequently, it was connected to wires at both ends and encapsulated with biomedical tape. Hydrogel fiber strain sensor was prepared by the same method.

Five hydrogel fiber strain sensors with a diameter of 1.2 mm were attached to the thumb, index, middle, ring and little fingers of a cotton glove for smart glove fabrication.

Characterization

The internal microstructure for hydrogels was characterized by using a scanning electron microscope at voltage of 100 kV. (SEM, Hitachi TM4000, Hitachi, Japan). The hydrogel samples were first swelled for 12 h to achieve equilibrium, then rapidly frozen in liquid nitrogen and freeze-dried thereafter. Attenuated total reflection Fourier-transform infrared spectroscopy was performed on the hydrogels using a spectrometer (Nicolet iS50, Thermo Fisher) in the range of 500 to 4000 cm^{-1}. An ultraviolet-visible (UV-Vis) spectrophotometer (UH4150, Hitachi, Japan) was used to characterize the transparency of the hydrogels within the wavelength range of 200 to 800 nm. A 200F3 DSC instrument (Germany) was used for differential scanning calorimetry (DSC) analysis, with a heating rate of 5 K min^{-1}, ranging from -80.0°C to 20.0°C, under a nitrogen atmosphere. The storage modulus (G′) and loss modulus (G″) of the hydrogel samples were measured using a modular compact rheometer (MCR302, Anton Paar GMBH, Austria) with an angular frequency sweep performed at a fixed strain of 1%, where the frequency was varied from 0.01 to 100 $rad \cdot s^{-1}$.

Environmental stability

The mass retention rates of the hydrogels at different time intervals were determined by the weighing method after the hydrogels were equilibrated for 12 h at a constant temperature of 20.0 °C and humidity of 40.0%. The mass ratio was defined as

$$Mass\ ratio\ (\%) = (M_i/M_0) \times 100\% \quad \text{(S1)}$$

where M_i and M_0 represent the mass of the hydrogel at different time points and its initial mass, respectively.

Mechanical measurement

Mechanical tensile tests were conducted on a universal testing machine (HY0580, Heng Yi, China). Unless otherwise specified, hydrogel samples with dimensions of 20.0 × 7.0 × 1.0 mm (length × width × thickness) were tested at 20.0 °C and 40.0% humidity with a tensile rate of 20 $mm \cdot min^{-1}$. Loading–unloading tensile curves were used to assess the dissipative energy and hysteresis of the hydrogels. Dissipative energy

(ΔE), defined as the area enclosed by the loading–unloading loop, was calculated according to the following formula:

$$(\int \sigma d\varepsilon)_{Loading} - (\int \sigma d\varepsilon)_{Unloading} \quad \text{(S2)}$$

The hysteresis was defined by the Equation as the following formula:

$$Hysteresis = \Delta E/(\int \sigma d\varepsilon)_{Loading} \quad \text{(S3)}$$

where σ and ε represent tensile stress and strain, respectively.

The tensile stress (σ) of hydrogels was defined by the Equation as the following formula:

$$\sigma = F/A \quad \text{(S4)}$$

where F was the load force recorded by the universal machine and A was the cross-sectional area of hydrogels.

The tensile strain (ε) of the hydrogel microfiber was defined by the equation as the following formula:

$$\varepsilon = (l - l_0)/l_0 \times 100\% \quad \text{(S5)}$$

where l_0 was the initial length of hydrogels between the fixtures and l was the length of hydrogels before breakage.

Conductivity measurement

The electrochemical workstation (CHI660E, Shanghai) was used to measure the electrochemical impedance spectroscopy of the hydrogel strain sensor, with a frequency range of 1.0 Hz to 1000 Hz and a voltage of 100.0 mV. Unless otherwise stated, the hydrogel strain sensor with 20.0 × 7.0 × 1.0 mm (length × width × thickness) was used for the electrical testing at a temperature of 20 °C and humidity of 40.0%. The ionic conductivity (σ, unit: S/m) was calculated according to the following equation:

$$\sigma = S/(LR) \quad \text{(S6)}$$

in which L (m), S (m^2), and R (Ω) are the length, cross sectional area and resistance of samples, respectively. R is obtained from the intercept at the real part in Nyquist plots.

The LCR tester (IM3536) recorded the resistance signal of the hydrogel strain sensor during deformation, where the applied voltage was 1.0 V and the frequency was 800.0 Hz. The relative resistance change ($\Delta R/R_0$) and Gauge factor (GF) were used to evaluate the sensing performance of the hydrogel strain sensor. The calculation formula was as follows:

$$\Delta R/R_0 = (R_s - R_0)/R_0 \quad \text{(S7)}$$

$$GF = (\Delta R/R_0)/\varepsilon \quad \text{(S8)}$$

where R_0 represented the original resistance before the application of strain, Rs represented the real-time resistance during the application of strain, and ε represented the strain. Measurement of the performance of hydrogel self-powered sensors by connecting the self-powered sensors with copper wire with a diameter of 1mm to an electrochemical workstation (CHI660E, Shanghai).

All experiments were conducted in triplicate unless stated otherwise. Error bars denote the standard deviation (SD), indicating the reproducibility and reliability of the experimental data.

Applications for hydrogel sensors and smart glove

The hydrogel, copper sheet (2.0 mm) and copper wires were assembled to make a strain sensor Attachment of hydrogel strain sensors to various body parts and fingers with medical adhesive tape.

Five hydrogel fibers were individually woven onto the five finger stalls of a cotton fabric glove and connected with copper wires to assemble a smart glove, which was then linked to a robotic hand manipulator via conductive wires and integrated with an Arduino Nano board. Prior to the experiment, the program code was pre-loaded into the Arduino Nano board, which read signals from the analog pins and transmitted them to convert the resistance variations of the smart glove into gesture control signals for the robotic manipulator.

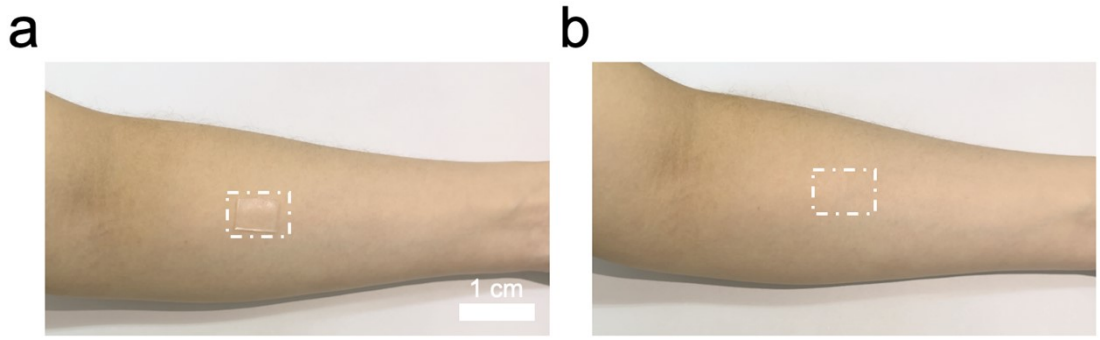

Fig. S1 The biocompatibility of the PAM/PVA/Tre/Li^+ hydrogel: (a) applied on human skin for 5 days, (b) skin condition after removal.

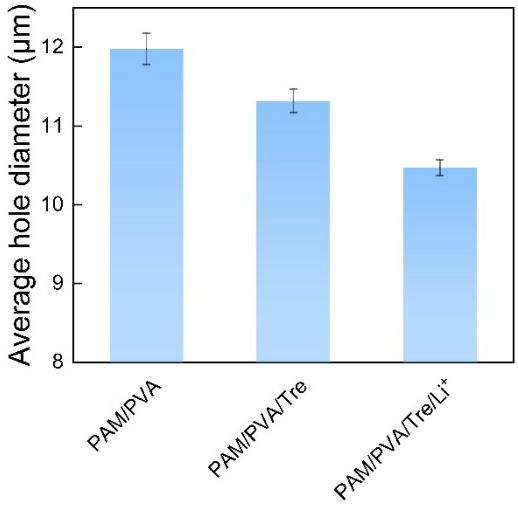

Fig. S2 Average hole diameter of the PAM/PVA, PAM/PVA/Tre, and PAM/PVA/Tre/Li^+ hydrogels.

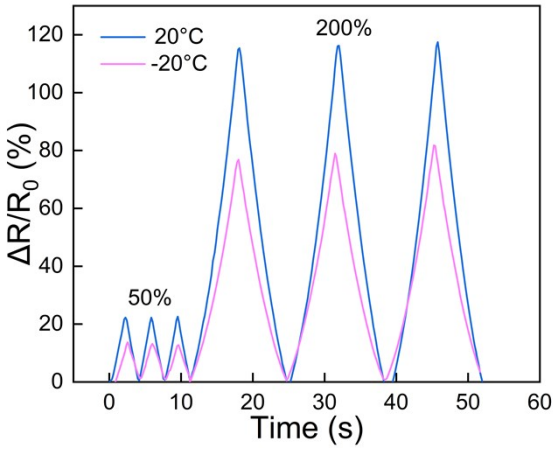

Fig. S3 Dynamic relative resistance responses of PAM/PVA/Tre/Li^+ hydrogels under 50.0% and 200.0% tensile strains at 20.0℃ and -20.0℃

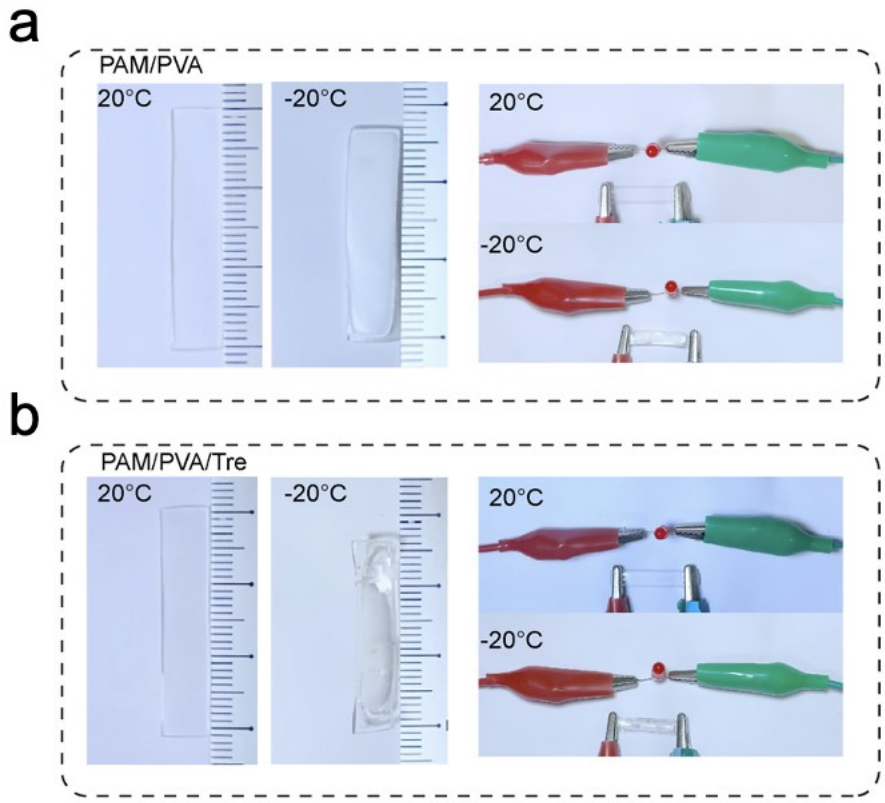

Fig. S4 Photographs of the state and conductivity tests for (a) PAM/PVA, and (b) PAM/PVA/Tre hydrogels at 20.0℃ and -20.0℃.

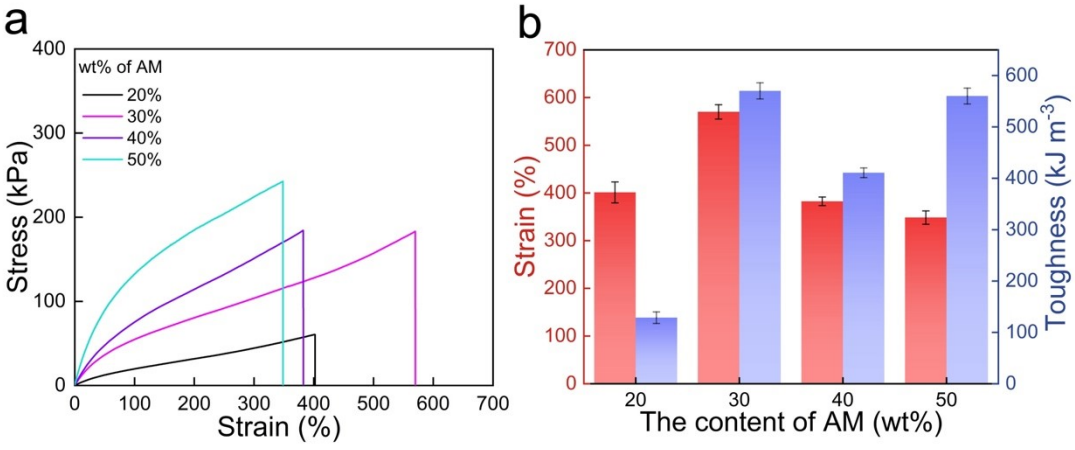

Fig. S5 (a) Tensile stress-strain curves of hydrogels with different content of AM. (b) The fracture strain and toughness of hydrogels with different content of AM.

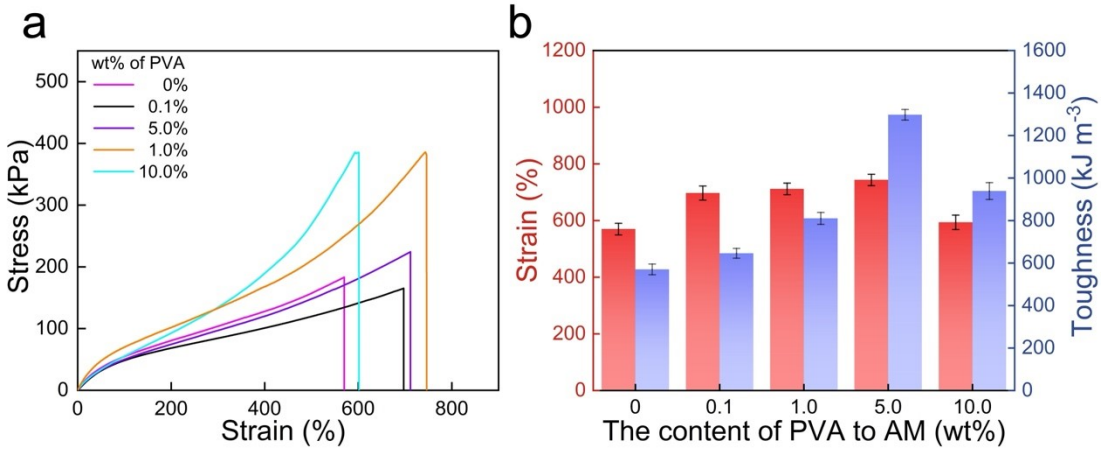

Fig. S6 (a) Tensile stress-strain curves of hydrogels with different content of PVA. (b) The fracture strain and toughness of hydrogels with different content of PVA.

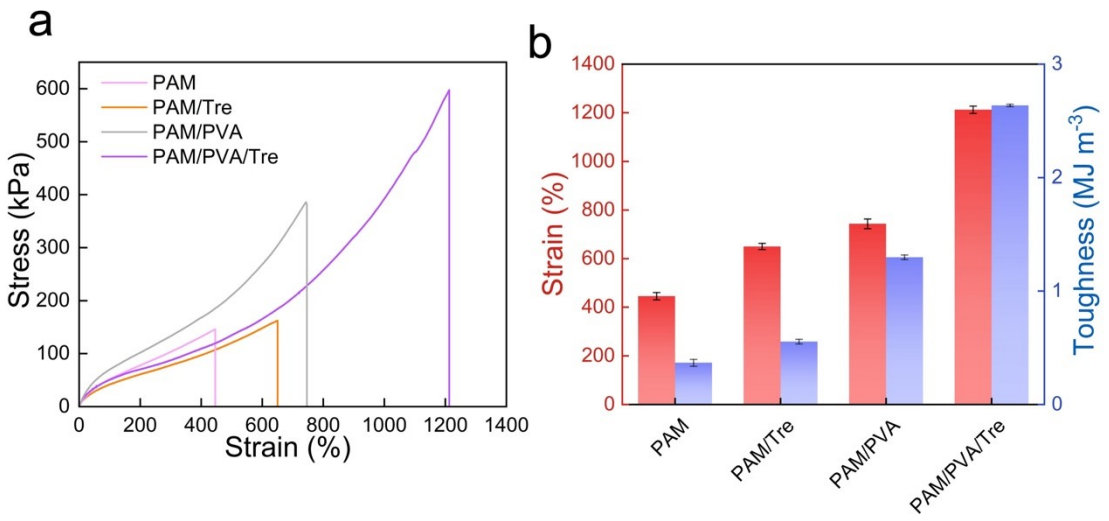

Fig. S7 Mechanical properties of hydrogels with different component combinations: (a) tensile stress-strain curves (b) fracture strain and toughness

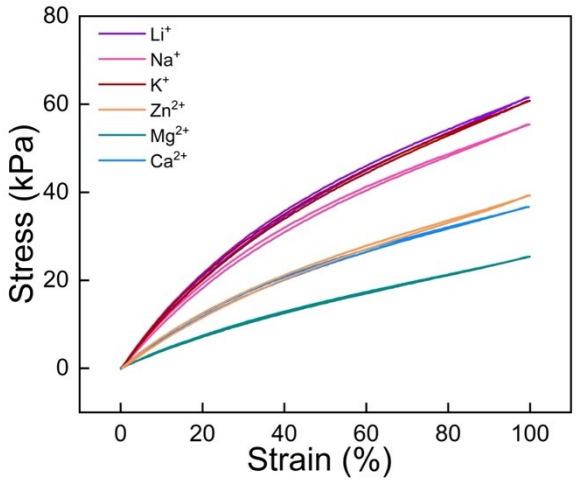

Fig. S8 Detailed stress-recovery curves and stability tests of hydrogels doped with different salts under 100.0% cyclic stretch.

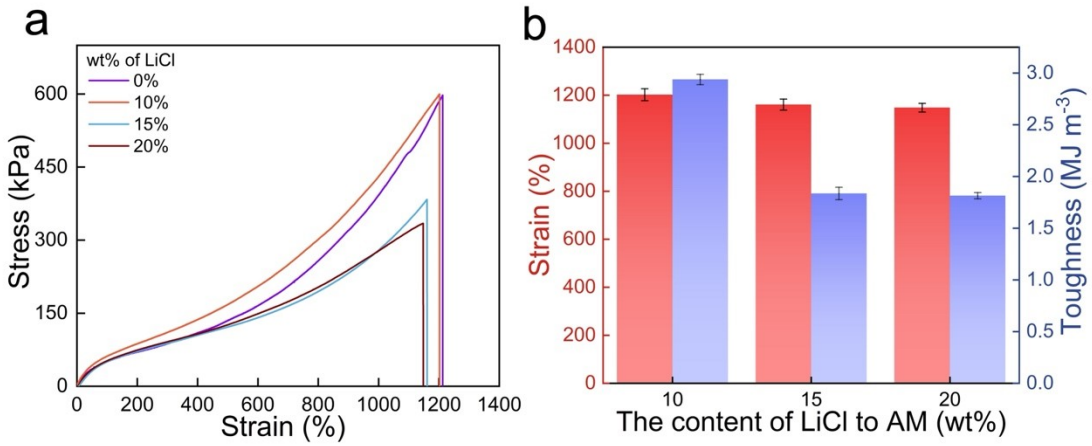

Fig. S9 (a) Tensile stress-strain curves of hydrogels with different content of LiCl. (b) The fracture strain and toughness of hydrogels with different content of LiCl.

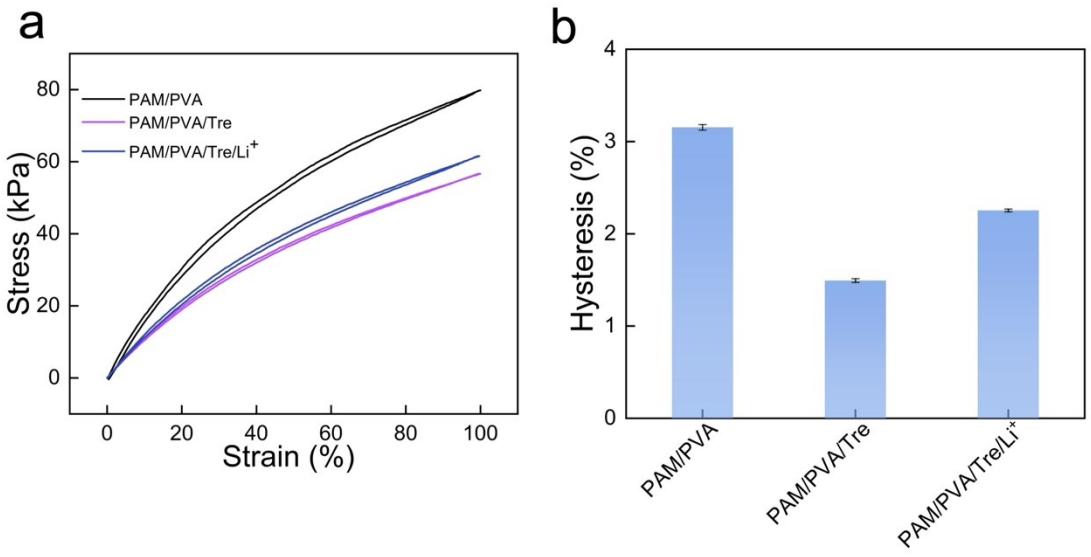

Fig. S10 Mechanical hysteresis behavior of hydrogels with different components: (a) loading-unloading stress-strain curves (b) hysteresis ratio

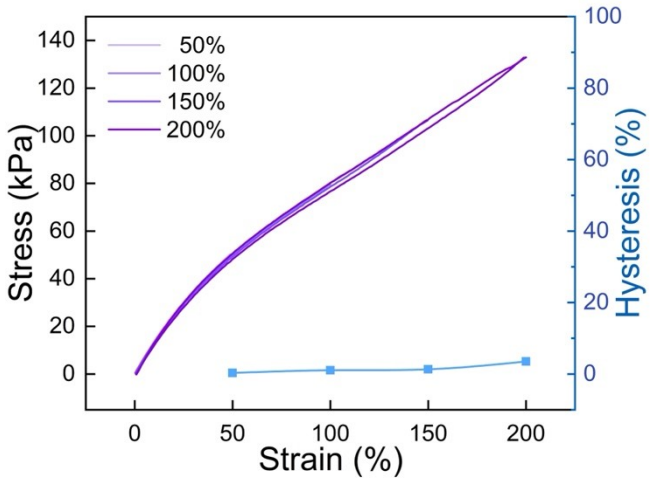

Fig. S11 Successive loading-unloading curves and mechanical hysteresis of the PAM/PVA/Tre/Li^+ hydrogel.

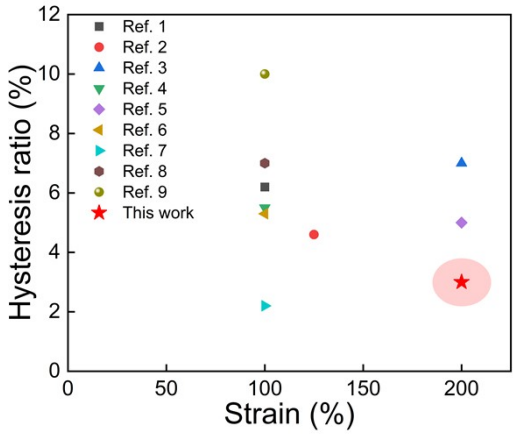

Fig. S12 Comparison of the hysteresis and strain of PAM/PVA/Tre/Li^+ hydrogels with those of previously reported hydrogels.

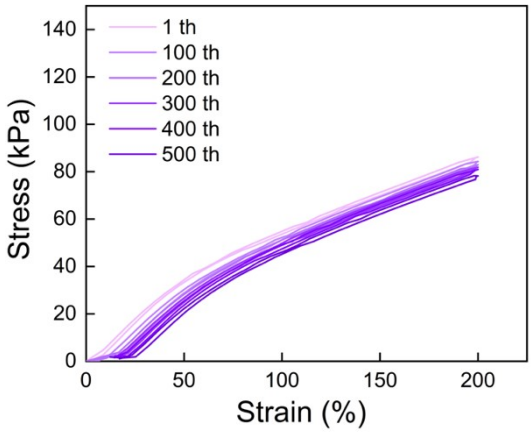

Fig. S13 Detailed stress-recovery curves and stability test of the PAM/PVA/Tre/Li^+ hydrogel under a cyclic stretch of 200.0% for 500 cycles.

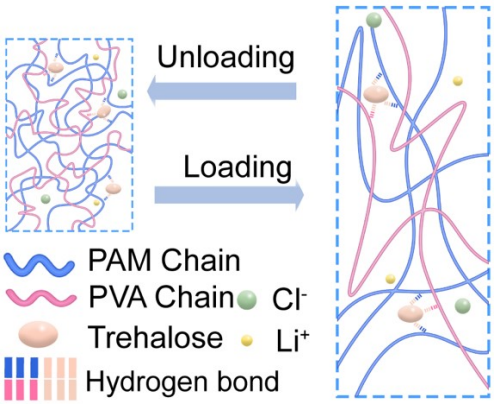

Fig. S14 Schematic illustration of the crosslinked network structure of the PAM/PVA/Tre/Li^+ hydrogel during the stretch-release cycle.

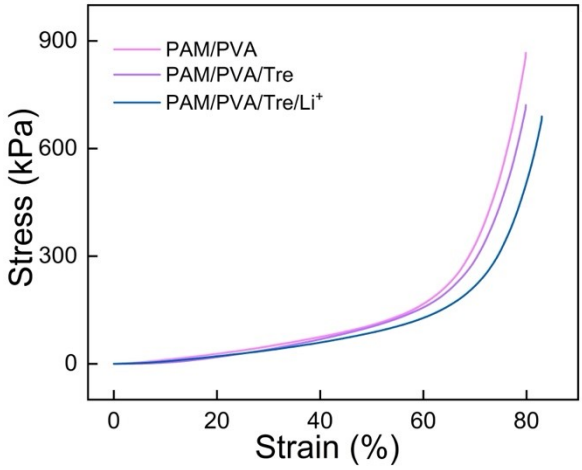

Fig. S15 Compressive stress-strain curves of PAM/PVA, PAM/PVA/Tre, and PAM/PVA/Tre/Li^+ hydrogels.

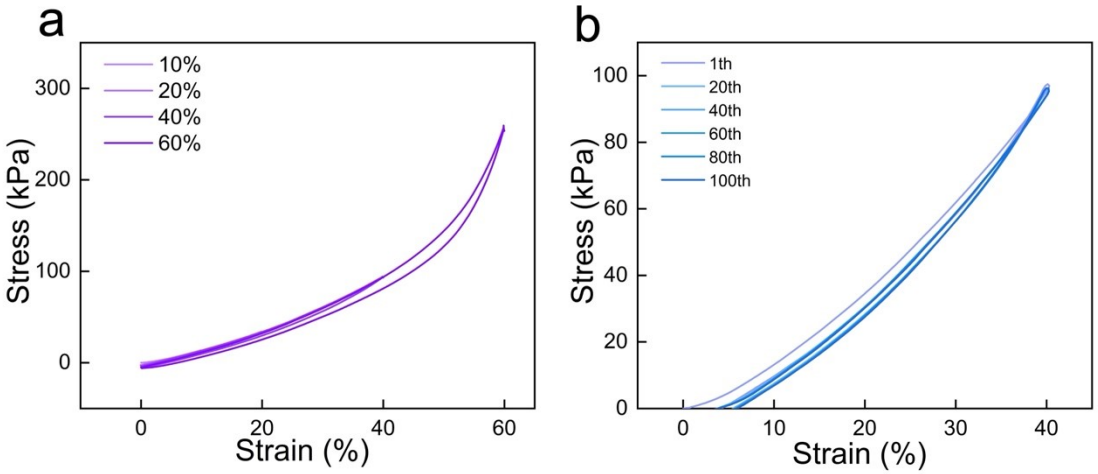

Fig. S16 (a) Stress-recovery curves of PAM/PVA/Tre hydrogel under different compression strains. (b) Cyclic compression test of PAM/PVA/Tre hydrogel under compression at the range of 0-40.0% over 100 cycles.

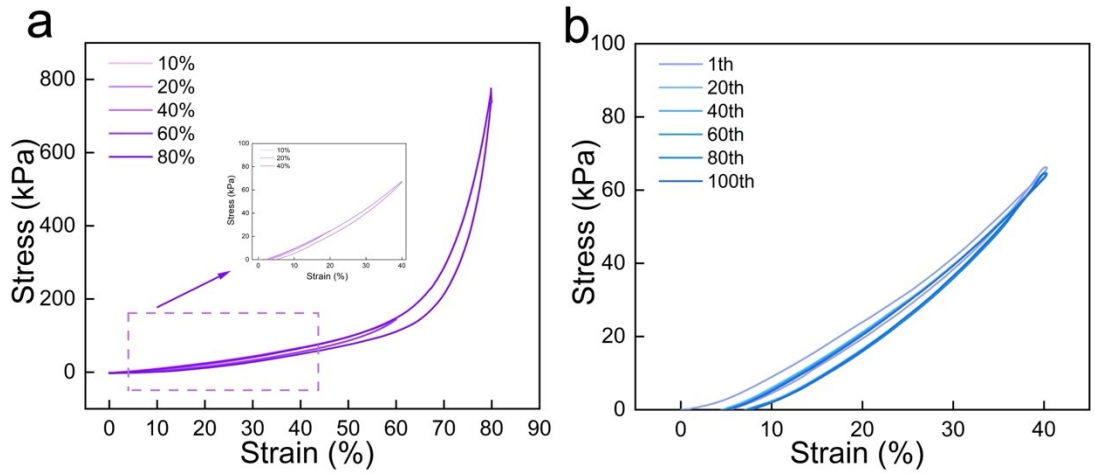

Fig. S17 (a) Stress-recovery curves of PAM/PVA/Tre/Li^+ hydrogel under different compression strains. (b) Cyclic compression test of PAM/PVA/Tre/Li^+ hydrogel under compression at the range of 0-40.0% over 100 cycles.

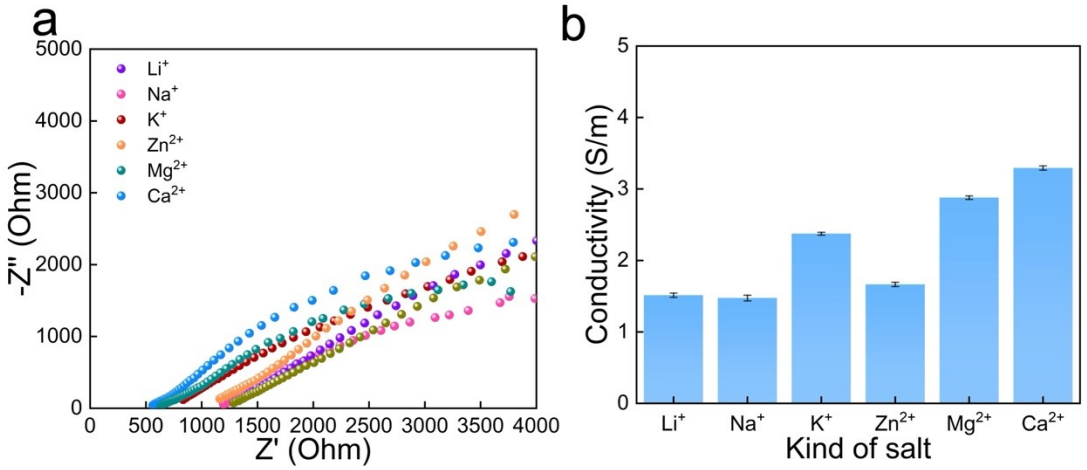

Fig. S18 (a) Electrochemical impedance spectroscopy (EIS) Nyquist plots and (b) corresponding ionic conductivity of hydrogels doped with different salts.

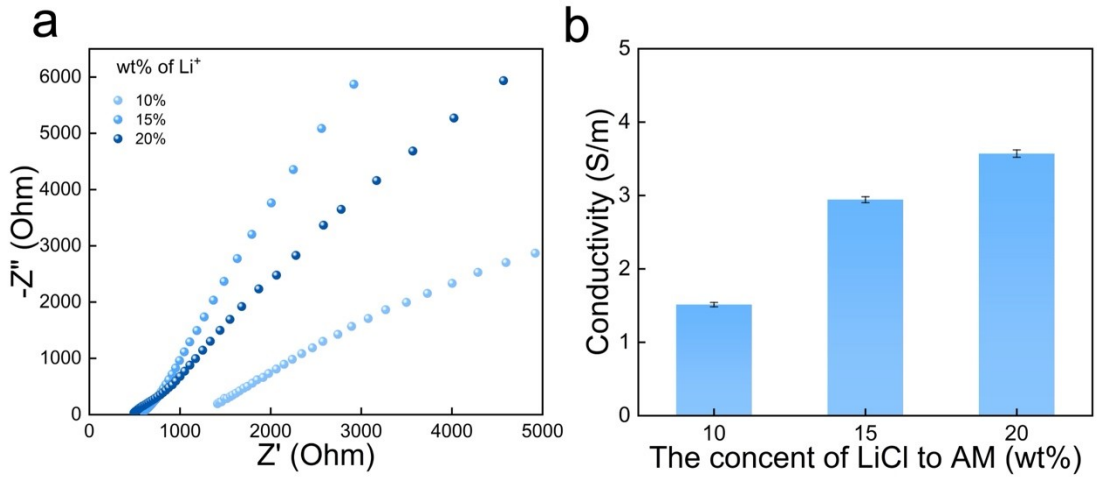

Fig. S19 (a) Electrochemical impedance spectroscopy (EIS) Nyquist plots and (b) corresponding ionic conductivity of hydrogels doped with different content of LiCl.

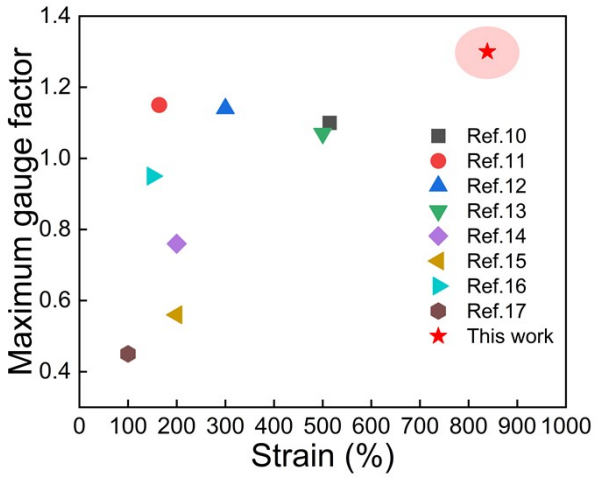

Fig. S20 Comparison of the maximum gauge factor of the PAM/PVA/Tre/Li^+ hydrogel sensor with those of previously reported hydrogels.

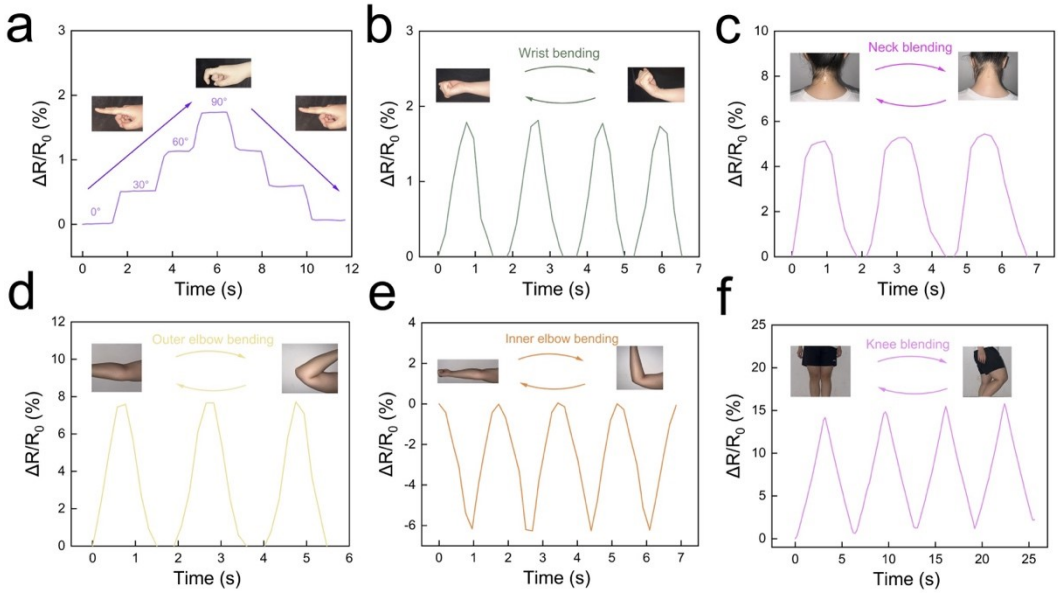

Fig. S21 Wearable applications of flexible resistive strain sensors based on PAM/PVA/Tre/Li^+ hydrogels. (a-d) Signal of relative resistance changes by bending finger, wrist, neck, elbow, and leg.

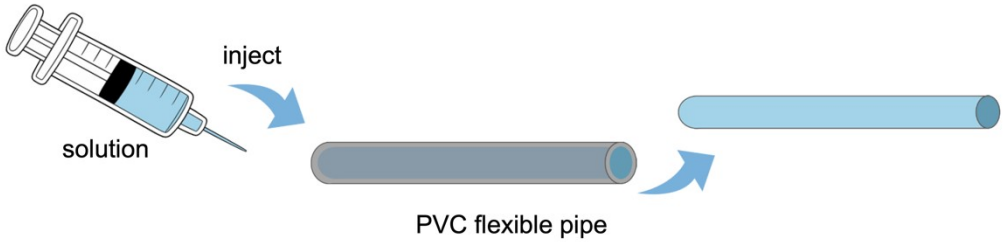

Fig. S22 Schematic illustration of hydrogel fiber preparation

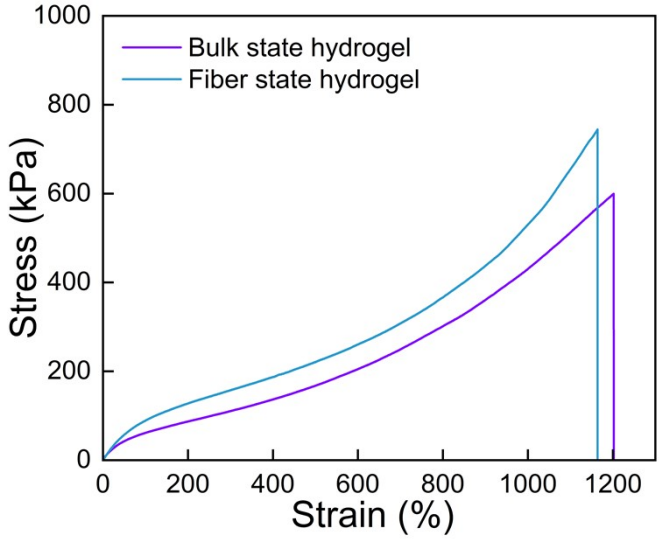

Fig. S23 Tensile stress-strain curves and mechanical performance of PAM/PVA/Tre/Li^+ hydrogels in bulk and fiber states.

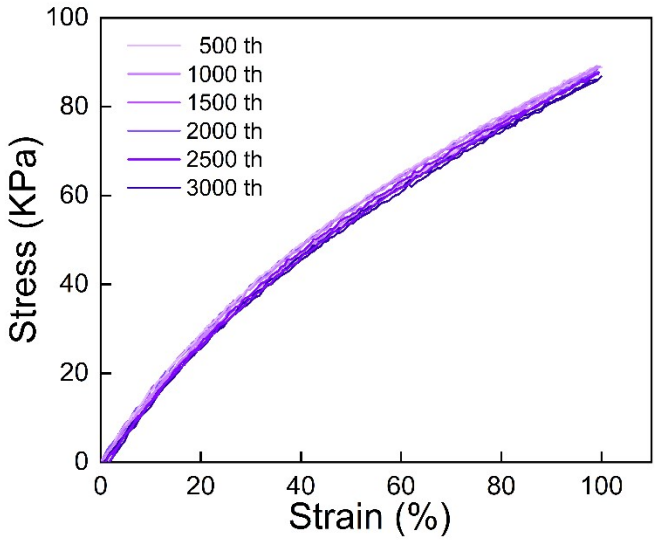

Fig. S24 Detailed stress-recovery curves and stability test of the fiber state hydrogel under a cyclic stretch of 100.0% for 3000 cycles.

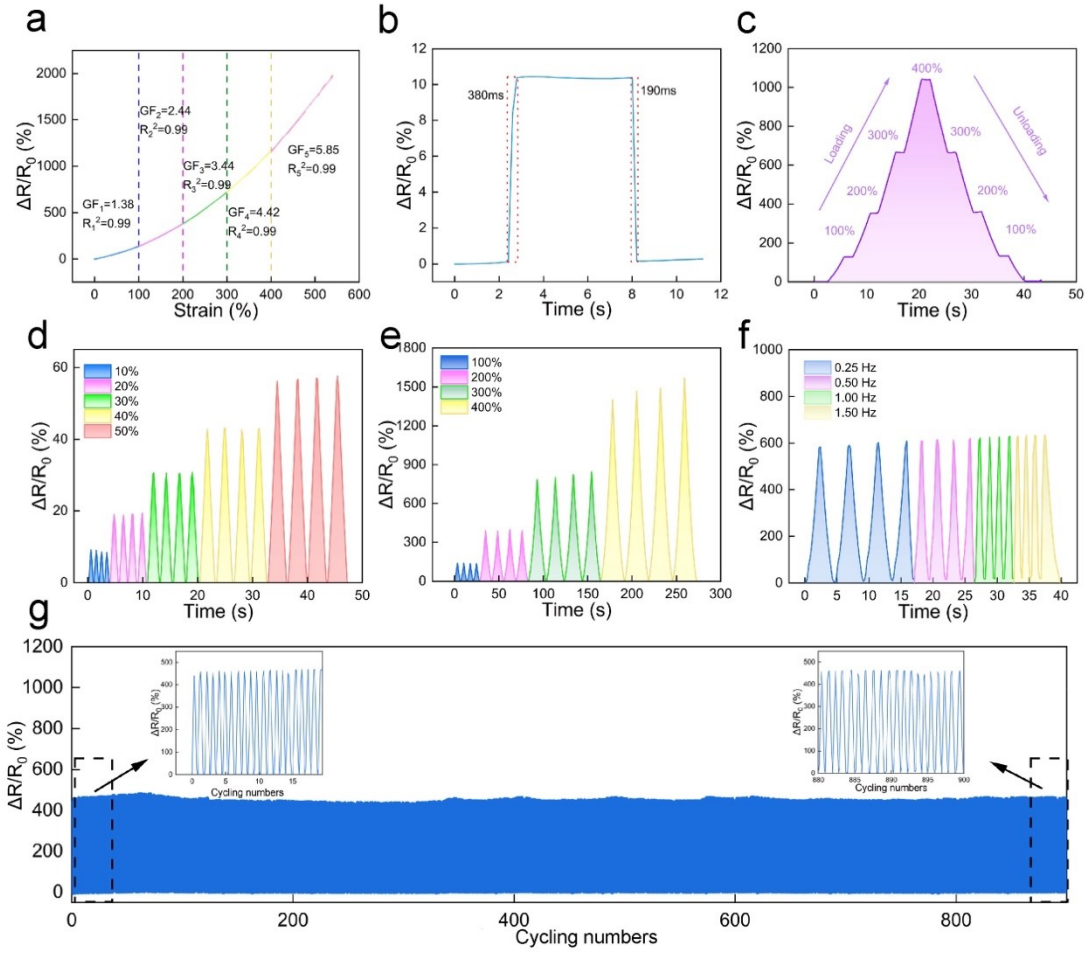

Fig. S25 (a) The relative resistance changes of the hydrogel fiber sensor as a function of strain. (b) Response and recovery times of the hydrogel fiber sensor. (c) The dynamic response of the hydrogel fiber sensor to sequential step-stretching of 100% and releasing back. (d-e) The relative resistance changes of the hydrogel fiber sensor during cyclic loading and unloading under small and large strains. (f) The relative resistance changes of the hydrogel fiber sensor during stretching to 200.0% strain at different strain frequency (from 0.25 Hz to 1.50 Hz). (g) The cycling sensing behavior of the hydrogel fiber sensor for 1000 cycles at a strain of 200.0%.

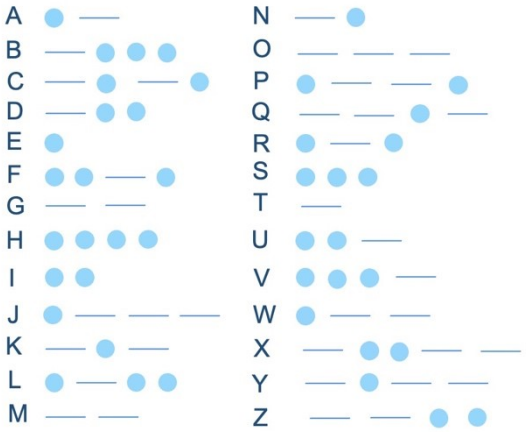

Fig. S26 Schematic diagram of communication transmission by Morse code.

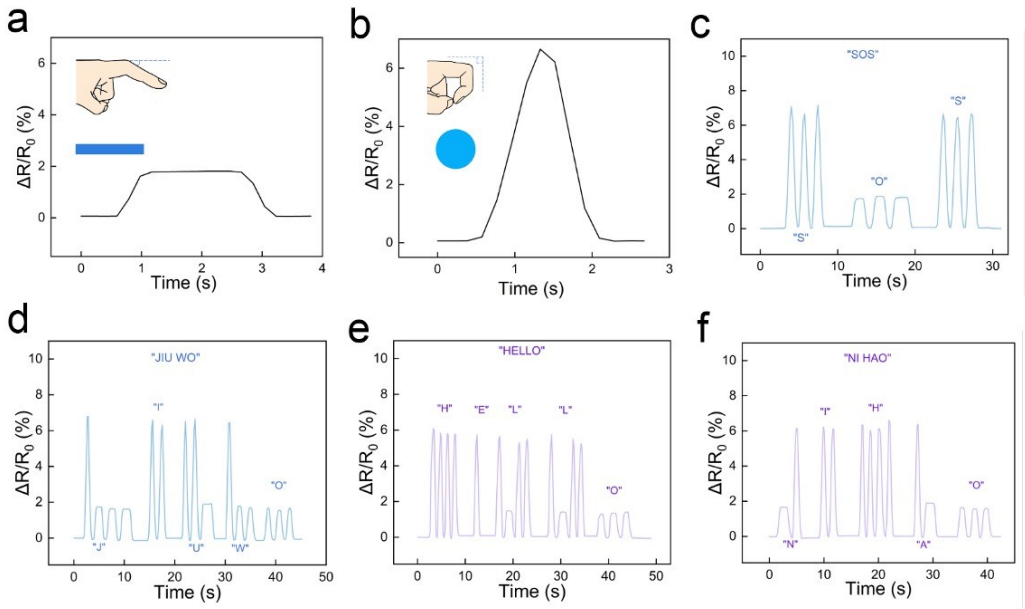

Fig. S27 Wearable applications of flexible resistive fiber sensors based on PAM/PVA/Tre/Li^+ hydrogels. (a and b) Signal of relative resistance changes of Morse code, where short lines represent bending angles from 90° to 30° and dots represent finger bending angles from 90.0° to 0° and (c-f) The hydrogel fiber sensor communicates through Morse code.

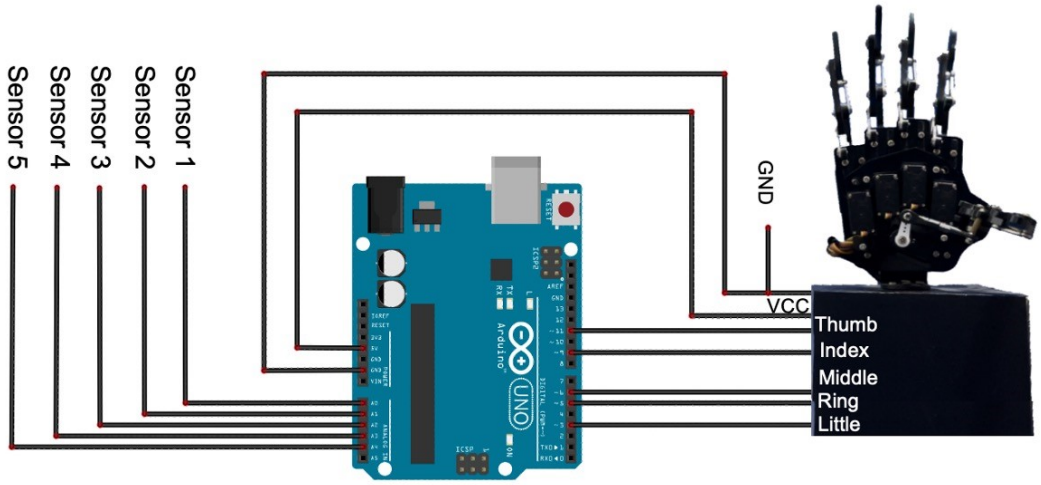

Fig. S28 Schematic illustration of the human-machine interaction system connection.

Table S1. Summary of performance results of reported conductive hydrogel.

Conductive component	Tensile strain (%)	Hysteresis (%)	Ref.
NaCl	100.0	6.2	1
/	125.0	4.6	2
CaCl2	200.0	7.0	3
NaCl	100.0	5.5	4
$[EMIm]^+[BF_4]^-$	200.0	5.0	5
PVA-SBQ	100.0	5.3	6
LiCl	100.0	2.2	7
MXene	100.0	7.0	8
LiCl	100.0	10.0	9
LiCl	200.0	3.0	This work

Table S2. Summary of performance results of reported conductive hydrogel.

Conductive component	Tensile strain (%)	Gauge factor (%)	Ref.
LiCl	514.2	1.1	10
LiCl	164.0	1.15	11
$ZnCl_2$	300.0	1.14	12
LiCl	500.0	1.07	13
AgNWs	200.0	0.76	14
PEDOT:PSS	200.0	0.56	15
NaCl	150.0	0.95	16
PANa	100.0	0.45	17
LiCl	800.0	1.30	This work

References

1. K. Lei, Q. Jiang, X. Wang and D. Gong, Macromol. Rapid Commun., 2025, 46, 2401134.
2. B. Zhang, J. Qiu, X. Meng, E. Sakai, H. Feng, L. Zhang, J. Tang, G. Zhang, H. Wu and S. Guo, ACS Appl. Mater. Interfaces, 2024, 16, 57769-57777.
3. L. Zhou, B. Zhao, J. Liang, F. Lu, W. Yang, J. Xu, J. Zheng, Y. Liu, R. Wang and Z. Liu, Mater. Horiz., 2024, 11, 3856-3866.
4. J. Xu, J. Liang, J. Zheng, F. Lu, Y. Ma, H. Yu, W. Zhao, R. Wang and Z. Liu, J. Mater. Chem. A, 2025, 13, 12256-12265.
5. S. Dai, C. Zhong, J. Yao, L. Zeng, Y. Zhong, S. Xie, W. Huang, W. Chen and Y. Sui, Colloids Surf., A, 2025, 710, 136212.
6. G. Lu, C. Li, G. Wang, J. Nie and X. Zhu, Sens. Actuators, A, 2023, 353, 114223.

7. Y. Wang, L. Song, Q. Wang, L. Wang, S. Li, H. Du, C. Wang, Y. Wang, P. Xue, W. C. Nie, X. Wang and S. Tang, Carbohydr. Polym., 2023, 318, 121106.
8. J. Zou, X. Jing, S. Li, P. Feng, Y. Chen and Y. Liu, Small, 2024, 20, e2401622.
9. Y. Zhao, Q. Zhao, S. Peng, H. Zhou and L. Yang, J. Mater. Chem. C, 2023, 11, 16135-16142.
10. X. Sun, F. Luo and F. Jiang, Macromol. Rapid Commun., 2025,
11. X. Pan, H. Zhu, F. Qin, M. Jing, H. Wu and Z. Sun, Sensors 2025, 25, 20250801.
12. H. Huo, H. Shi, H. Yang, X. Zhang, J. Wan, J. Shen, G. Du and L. Yang, J. Mater. Chem. A, 2024, 12, 27506-27517.
13. D. Cui, Y. Sun, T. Li, Z. Hu, Y. Zhao, X. Wang, S. Chen, Z. Toktarbay and H. Wei, Adv. Compos. Hybrid Mater., 2025, 8, 233.
14. S. Azadi, S. Peng, S. A. Moshizi, M. Asadnia, J. Xu, I. Park, C. H. Wang and S. Wu, Adv. Mater. Technol. , 2020, 5, 2000426.
15. J. Zhou, J. Zheng, C. Wang, M. Fan, S. Wang, F. Xiong, Y. Li and C. Yang, RSC Adv., 2026, 16, 1240-1254.
16. H. Wu, Y. Wu, J. Yan, W. Xiao, Y. Wang, H. Zhang, X. Huang, H. Xue, L. Wang, L. Tang, Y. Mai and J. Gao, Chem. Eng. J. , 2024, 488, 150963.
17. S. Zhang, Y. Li, H. Zhang, G. Wang, H. Wei, X. Zhang and N. Ma, ACS Mater. Lett., 2021, 3, 807-814.